THE JOURNAL OF PHYSICAL CHEMISTRY C

Article

pubs.acs.org/JPCC

Structure and Conductivity of Epitaxial Thin Films of In-Doped $BaZrO_3$-Based Proton Conductors

Laura Mazzei,[†] Max Wolff,[‡] Daniele Pergolesi,[§] Joseph A. Dura,[∥] Lars Börjesson,[†] Philipp Gutfreund,[⊥] Marco Bettinelli,[#] Thomas Lippert,[§,¶] and Maths Karlsson*[,†]

[†]Department of Physics, Chalmers University of Technology, SE-412 96 Göteborg, Sweden

[‡]Department of Physics and Astronomy, Uppsala University, 75120 Uppsala, Sweden

[§]Energy and Environment Research Division, Paul Scherrer Institute, 5232 Villigen, PSI, Switzerland

[∥]NIST Center for Neutron Research, National Institute of Standards and Technology, Gaithersburg, Maryland 20899-6102, United States

[⊥]Institut Laue-Langevin, 71 Avenue des Martyrs, 38000 Grenoble, France

[#]Luminescent Materials Laboratory, University of Verona, 37134 Verona, Italy

[¶]Department of Chemistry and Applied Biosciences, Laboratory of Inorganic Chemistry, Vladimir-Prelog-Weg 1-5/10, ETH Zürich, Zürich CH-8093, Switzerland

Supporting Information

ABSTRACT: Epitaxial thin films of the proton-conducting perovskite $BaZr_{0.53}In_{0.47}O_{3-\delta}H_{0.47-2\delta}$, grown by pulsed laser deposition, were investigated in their hydrated and dehydrated conditions through a multitechnique approach with the aim to study the structure and proton concentration depth profile and their relationship to proton conductivity. The techniques used were X-ray diffraction, X-ray and neutron reflectivity, nuclear reaction analysis, and Rutherford backscattering, together with impedance spectroscopy. The obtained proton conductivity and activation energy are comparable to literature values for the bulk conductivity of similar materials, thus showing that grain-boundary conductivity is negligible due to the high crystallinity of the film. The results reveal an uneven proton concentration depth profile, with the presence of a 3−4 nm thick, proton-rich layer with altered composition, likely characterized by cationic deficiency. While this surface layer either retains or reobtains protons after desorption and cooling to room temperature, the bulk of the film absorbs and desorbs protons in the expected manner. It is suggested that the protons in the near-surface, proton-rich region are located in proton sites characterized by relatively strong O−H bonds due to weak hydrogen-bond interactions to neighboring oxygen atoms and that the mobility of protons in these sites is generally lower than in proton sites associated with stronger hydrogen bonds. It follows that strongly hydrogen-bonding configurations are important for high proton mobility.

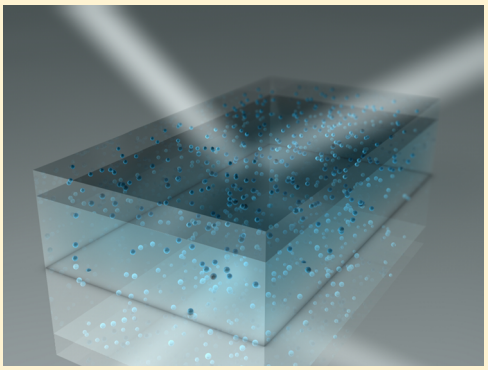

1. INTRODUCTION

Perovskite type oxides, of the form ABO_3, where A and B are cations and O is oxygen, exhibit many interesting properties due to their ability to accommodate a large range of variations: cations, substitution (doping), nonstoichiometry, and structural defects. Of specific concern for this work are acceptor-doped, hydrated perovskites, which currently are of large interest because of their potential usage as electrolytes in future environmentally friendly solid oxide fuel cells (SOFCs).[1,2] The role of the acceptor doping, such as In^{3+} substituted for Zr^{4+} in $BaZrO_3$, is to create an oxygen-deficient structure ($BaZr_{1-x}In_xO_{3-x/2}$, where x refers to the doping level), which can be hydrated by heat treatment in a humid atmosphere.[2,3] During this process, water molecules from the gaseous phase dissociate on the surface of the sample into hydroxyl groups (OH^-) and protons (H^+). The hydroxyl groups occupy nearby oxygen vacancies, while the remaining protons bind to oxygens of the perovskite host lattice. The protons can diffuse (jump) from one oxygen to another, and with time, they diffuse into the bulk of the material. At the same time as protons diffuse into the bulk, the counter diffusion of oxygen vacancies from the bulk to the surface of the sample allows the dissociation of other water molecules. This leads to an increase of the proton concentration in the material, and ideally, this process continues until the (bulk) oxygen vacancies are filled, leading to a fully hydrated structure, i.e., $BaZr_{1-x}In_xO_3H_x$.

However, there are aspects related to the proton loading mechanism, proton distribution, and proton diffusion in these

Received: August 24, 2016
Revised: October 6, 2016
Published: November 1, 2016

DOI: 10.1021/acs.jpcc.6b08570
J. Phys. Chem. C 2016, 120, 28415−28422

materials that are still unclear. For instance, it has appeared difficult to fully hydrate (protonate) many of these systems. A survey of the literature shows that the degree of protonation usually varies between 60% and 100%,[3−11] irrespective of using different types of experimental conditions, e.g., temperature, level of relative humidity, and time, but sometimes even values well above 100% have been found.[12] The occurrence of an incomplete or excess protonation is an interesting fact pointing toward the likelihood of an uneven distribution of protons in the material. Moreover, an incompletely hydrated structure ($BaZr_{1-x}In_xO_{3-\delta}H_{x-2\delta}$) inherently contains unfilled oxygen vacancies, which leads to the formation of a variety of different local proton sites, manifested by, for example, the very broad O−H stretch band in the infrared (IR) absorbance spectra that is generally observed for these materials.[3,4,13] As our knowledge about the local (short-range) structure of proton-conducting perovskites has advanced, it has become clear that the supposedly simple task of elucidating the mechanistic aspects of proton transport in oxides is a very challenging one. In particular, the presence of dopant atoms,[10,14−16] oxygen vacancies,[17,18] and other structural defects complicates the description of the atomic-scale proton dynamics, and yet it is not fully understood for even the simplest materials. Further, for the application of proton-conducting oxides in miniaturized SOFCs, which are currently accumulating increased attention, one would use a film ($\lesssim$1 μm) of the proton conductor sandwiched between the anode and cathode.[19,20] Differently from powder samples, such films represent a confined state and furthermore can be textured, strained, and exhibit varying degrees of crystallinity, which may affect significantly the performance of the electrolyte.[21−23] Developing a thorough understanding of the structure and coordination of protons in proton-conducting oxides (bulk and thin films) is therefore particularly important for the further development of SOFC technology and for other electrochemical devices using proton-conducting oxides, such as hydrogen sensors and steam electrolyzers,[24] to name a few.

In this work, we investigate the structure, proton concentration depth profile, and conductivity of epitaxial thin films of $BaZr_{0.53}In_{0.47}O_{3-\delta}H_{0.47-2\delta}$. The choice of material combines an average cubic structure with a high proton concentration and proton mobility upon hydration[5,6,13,14,25−27] and therefore serves as an excellent model system for studying chemical composition−structure−conductivity relationships in proton-conducting oxides. In particular, we examine nominally (fully) hydrated samples and investigate in detail any possible degradation effects upon dehydration, which would be applicable to fuel cells in actual operations. The investigations are performed through a multitechnique approach, using X-ray diffraction (XRD), X-ray and neutron reflectivity (XRR and NR), nuclear reaction analysis (NRA), and Rutherford backscattering (RBS), together with impedance spectroscopy (IS). Whereas XRR, NR, and NRA are well-established concentration profiling techniques of thin-film materials generally, they have not before been employed in studies of proton-conducting oxides. Our results reveal an uneven proton concentration depth profile, with the presence of a 3−4 nm thick surface, proton-rich layer with altered composition, likely characterized by cationic deficiency. While this surface layer either retains or reobtains protons after desorption and cooling to room temperature, the bulk of the film absorbs and desorbs protons in the expected manner. The implications of these results are discussed in view of the mechanism of proton conduction.

2. EXPERIMENTAL DETAILS

2.1. Sample Preparation and Characterization. Thin films (≈50 nm) of a nominal composition of $BaZr_{0.5}In_{0.5}O_{2.75}$ were grown by pulsed laser deposition (PLD) using a KrF excimer laser (Coherent Lambda Physik GmbH)[28] with a wavelength of 248 nm and a pulse width of 25 ns. A sintered ceramic pellet of $BaZr_{0.5}In_{0.5}O_{2.75}$, obtained by spark plasma sintering, was used as target material for the PLD. The substrates, (100)-oriented 10 × 15 × 0.5 mm^3 MgO (CrysTec GmbH), were ultrasonically cleaned in acetone and isopropanol before the deposition. The use of (100)-oriented MgO as substrate material is motivated by the excellent lattice matching between the cubic perovskite structure of $BaZr_{0.5}In_{0.5}O_{2.75}$ (4.20 Å)[6,25,29] and the cubic rock-salt structure of MgO (4.21 Å). This allows minimizing the lattice strain at the film/substrate interface.

The laser was focused on a spot size of about 3 mm^2 on the surface of the target, with an energy of 40 mJ (measured at the target) and a repetition rate of 2 Hz, and the target to substrate distance was 70 mm. The custom-made vacuum chamber was evacuated to a base pressure of 10^{-8} mbar, and a gas inlet line allows setting the required oxygen partial pressure to 0.002 mbar during the growth. A radiant heater sets the deposition temperature of the substrate holder. The deposition temperature was set to 730 °C and monitored by a pyrometer. To ensure good thermal contact with the heating plate and accurate temperature reading, platinum paste was applied between the heating plate and the substrate. The temperature was monitored at the platinum paste using the platinum black emissivity value of 0.97. In this experimental condition a deposition rate of about 0.08 Å s^{-1} was measured by XRR. The deposition was followed by a post annealing of 20 min in an oxygen partial pressure of about 10 mbar performed *in situ* at the same temperature set during the growth. The crystalline structure of the as-grown films was investigated by XRD performed on a Siemens D500 diffractometer.

Hydrated and deuterated films were prepared by annealing the as-grown films during slow (48 h) cooling from 400 to 200 °C, under a flow of N_2 saturated with water and heavy water, respectively. A dehydrated (dry) sample was prepared by annealing one of the as-grown films at 700 °C in vacuum (10^{-4} mbar) for about 1 day. The bulk atomic composition of a dehydrated film was determined by RBS using 2 MeV ^{4}He ions and a scattering angle of 165°.

2.2. Impedance Spectroscopy Measurements. The IS measurements of the proton conductivity were performed in a tubular furnace between 260 and 600 °C under a flow of humidified Ar. Two parallel strip-shaped Pt electrodes about 100 nm thick were deposited on the film. Ag paste and Au wires were used for the electrical connection to the impedance/gain-phase analyzer (Solartron 1260). A bias voltage of 1 V was used in the frequency range between 1 Hz and 1 MHz. Data analysis was performed with EC-Lab (V10.31). The data were fit to the response of an RC parallel circuit.

2.3. X-ray and Neutron Reflectivity Measurements. The XRR measurements were performed on two separate samples, one nominally dehydrated and the other hydrated, using a PANalytical X-ray diffractometer. The X-ray beam was reflected from the sample and detected at the specular condition as a function of scattering vector perpendicular to

DOI: 10.1021/acs.jpcc.6b08570
J. Phys. Chem. C 2016, 120, 28415−28422

the sample surface, $Q_z = (4\pi/\lambda)\sin\theta$, where θ is the incident and reflected angle and λ is the wavelength of the incident photons (λ = 1.54 Å). The incident beam divergence was 1/32°. The measurements were performed under ambient conditions. Data reduction and analysis of the reflectivity data were performed using the GenX software.[30]

The NR measurements were performed using two different instruments on a single sample in its nominally hydrated, deuterated, and dehydrated states. A first set of data was measured at the NIST Center for Neutron Research on the vertical sample geometry polarized beam reflectometer (PBR),[31] using neutrons of a wavelength of λ = 4.786 Å. Scattering angles were in the range $0.15° \leq \theta \leq 4°$, giving access to a Q-range of 0.007−0.18 Å^{-1}. The nominally fully hydrated sample was mounted on a heating stage inside a vacuum chamber (10^{-6} mbar), and the measurements were performed first at room temperature and thereafter at 400 °C. At the experimental conditions of 400 °C and 10^{-6} mbar the sample can be expected to be dehydrated. Data reduction and analysis of the NR data were performed using the reflpak software.[32] A second set of data was measured at the Institut Laue-Langevin on the vertical sample geometry D17 reflectometer, using nonpolarized neutrons and the time-of-flight (TOF) configuration.[33] First, the reflectivity of the sample in a fully deuterated condition was measured. Second, the sample was measured, at room temperature, in its dehydrated condition, which was obtained *in situ* by 4 h heat treatment in vacuum (400 °C, 10^{-6} mbar). All measurements were performed at room temperature under vacuum and taken at scattering vectors $0.01 \text{ Å}^{-1} \leq Q_z \leq 0.2 \text{ Å}^{-1}$. Data reduction and analysis of the D17 data were performed using the motofit package.[34]

Specular XRR and NR measurements probe the electron and the neutron scattering length density (SLD) profile along the normal to the surface of the sample. In the case of XRR, the electron SLD is defined as

$$e\text{SLD}(z) = \sum_{i=1}^{m} f_i \rho_i(z) \tag{1}$$

where $\rho_i(z)$ is the number density of the atomic species i as a function of depth (z) and f_i is its atomic scattering factor. Differently from X-rays neutrons interact with the atomic nuclei rather than the atoms' electrons; therefore, the neutron SLD is defined as

$$n\text{SLD}(z) = \sum_{i=1}^{m} b_i \rho_i(z) \tag{2}$$

where b_i is the coherent neutron scattering length of the isotope i. At each interface of the sample part of the wave amplitude is reflected and refracted and, for a layered structure, the constructive interference of the reflected waves is found at Q_z fulfilling the Bragg condition, $n\lambda = 2d \sin\theta$, where n is an integer number and d the thickness of the layer. Alternatively, this condition can be expressed as

$$Q_z = \frac{4\pi \sin\theta}{\lambda} = n\frac{2\pi}{d} \tag{3}$$

The interference of the waves reflected from the different interfaces of a film gives rise to fringes in $R(Q_z)$, referred to as Kiessig fringes.[35] Roughness at the surface/interfaces of the sample leads to a steeper decay of $R(Q_z)$ and a damping of the Kiessig fringes. In this work we used recursive fitting routines similar to the Parrat formalism.[36] With this approach it is possible to fit both the eSLD(z) and nSLD(z) to experimental data. We also exploit the fact that X-rays and neutrons exhibit very different sensitivities to the same atomic species, which results in the possibility to use XRR and NR as complementary techniques. We use XRR to determine the composition depth profile of the perovskite host, while NR is used to obtain details about the composition depth profile of the hydrogen and deuterium atoms, [H](z) and [D](z). This can then be compared with the results of the NRA measurements, as described below.

2.4. Nuclear Reaction Analysis Measurements. NRA measurements were performed in order to determine [H](z) in the nominally hydrated and dehydrated films as used in the XRR measurements. The measurements were performed at the Tandem Accelerator at Uppsala University using a beam of ^{15}N atoms with energies in the range E = 6.36−7 MeV. ^{15}N ions have a narrow nuclear resonant reaction with hydrogen at the resonant energy of E_R = 6.385 MeV, expressed by $^1\text{H} + {}^{15}\text{N} \rightarrow {}^{12}\text{C} + \alpha + \gamma$. The resulting gamma ($\gamma$) count rate was detected by NaI scintillators and is directly proportional to the hydrogen concentration, [H].

Depth resolution was achieved by using ^{15}N ions of energy $E > E_R$. These ions penetrate into the sample and decelerate until they reach, at a certain depth z, the resonance energy E_R, where the deceleration of the ions is related to the interaction with electrons in the material. This depth can be calculated as $z = (E - E_R)/S$, where S is the stopping power or energy loss per nanometer.[37] Since we are dealing with relatively thin films on substrates which do not contain hydrogen, S can be extracted from the knowledge of the total thickness d of the film and the energy E_d such that ions with energy $E > E_d$ will pass through the whole film without interaction with any hydrogen. The stopping power can be estimated as $S = (E_d - E_R)/d$. The resolution for the energy of the ^{15}N beam was approximately 13 keV [see Figure S1 in the Supporting Information (SI)], which corresponds to a depth resolution in the film of approximately 50 Å. In our experiment, the NR measurements provide an independent assessment of the average bulk hydrogen content; hence, as will be explained in further details, we used the results from NR to estimate the absolute hydrogen content from the NRA measurements.

3. RESULTS

3.1. X-ray Diffraction and Rutherford Backscattering. Figure 1 shows the XRD pattern as measured for an as-grown film, together with tick marks which indicate the positions of the Bragg peaks predicted by structural models based on the $Pm\bar{3}m$ symmetry of $BaZrO_3$. The (100) and (200) peaks of the perovskite material are clearly visible, where the latter one overlaps with the (200) reflection of the MgO substrate due to the small lattice mismatch between the film and substrate material. Note that no other reflections, such as (110) and (110), are observed, which shows that the film is (100)-epitaxially oriented, as expected.

The bulk atomic compositions, determined by the RBS measurements, were found to be 22.3(±1)% (Ba), 11.9(±1)% (Zr), 10.4(±1)% (In), and 55.4(±1)% (O); the RBS spectrum is shown in Figure S2. This corresponds to a doping level of x = 0.47, and consequently, the samples are hereafter labeled as 47In:BZO. It should be noted that whereas the obtained cationic content is in agreement with the expected composition the anionic (oxygen) content per unit formula is lower than

DOI: 10.1021/acs.jpcc.6b08570
J. Phys. Chem. C 2016, 120, 28415−28422

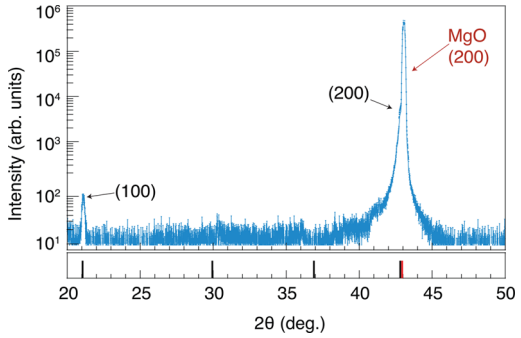

Figure 1. XRD pattern for a thin film of In-doped $BaZrO_3$, on a (100) oriented MgO substrate, together with tick marks which indicate the predicted positions of the (100), (110), (111), and (200) reflections. The red-colored tick mark is the position of the (200) reflection for MgO.

expected. Nonstochiometric, additional oxygen vacancies may appear as a consequence of the reduction of the cations in the perovskite structure during heat treatment.

3.2. Proton Conductivity. Figure 2 shows heating and cooling curves of the conductivity as a function of temperature,

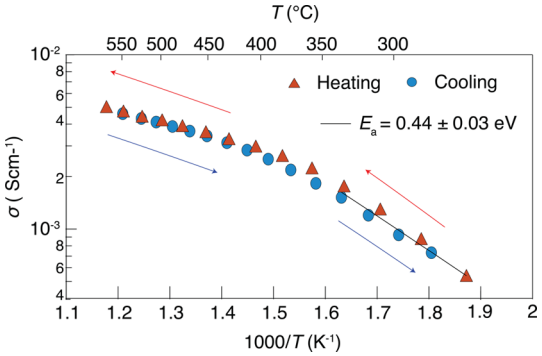

Figure 2. Conductivity data of the 47In:BZO thin film, as measured in a wet atmosphere upon heating (260 → 600 °C) followed by cooling (600 → 260 °C). The activation energy was obtained from the fit, indicated with the black line, of the data between 260 and 340 °C.

$\sigma(T)$, as extracted from the IS measurements. The proton conductivity shows an Arrhenius-like temperature dependence for $T \lesssim 350$ °C. At higher temperatures, the conductivity deviates from this Arrhenius behavior, in agreement with the initiation of the dehydration of the material.[6] The two curves are overall very similar, and the small differences in the measurements upon heating and cooling can be ascribed to possible small differences in proton concentration.

The obtained proton conductivity, 9.2×10^{-4} S cm^{-1} (at 300 °C), and activation energy, 0.44 eV, are comparable to the bulk proton conductivities and activation energies for powder samples of similar materials, e.g., 8.9×10^{-4} S cm^{-1} (at 300 °C) and 0.4 eV for $BaZr_{0.25}In_{0.75}O_{2.625}$.[6] Thus, we can assume that the grain boundary (GB) contribution to the conductivity, which would lower the proton conductivity by at least 1 order of magnitude,[6,9,25] is negligible in our samples. This is ascribed to the high crystalline quality of the film, in agreement with our XRD results.

3.3. X-ray Reflectivity and *e*SLD Profiles. Figure 3(a) shows the reflected intensities, plotted as a function of the scattering vector Q_z, for both the hydrated sample and the dehydrated sample. The Kiessig fringes correspond to a total

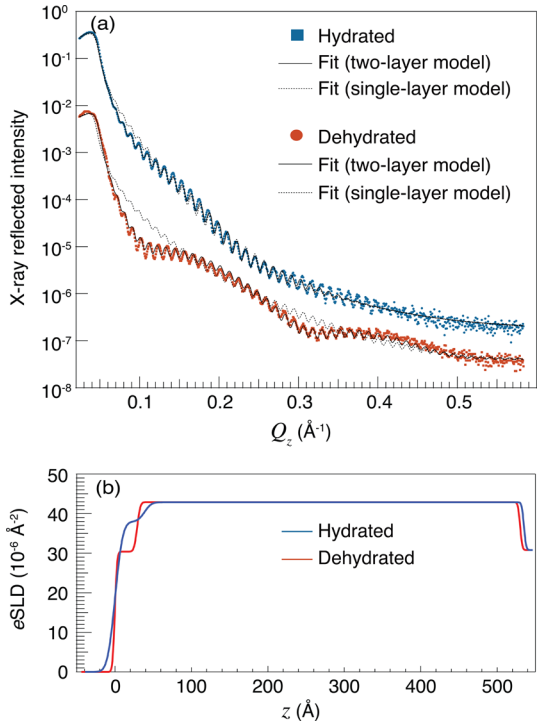

Figure 3. (a) Reflected X-ray intensity data and best fits to the data using a two-layer and single-layer model, respectively, for the hydrated and dehydrated 47In:BZO films. (b) *e*SLD profiles obtained from the fits based on the two-layer model. The data for the dehydrated sample in (a) have been scaled by 1 order of magnitude for clarity.

thickness of the film of approximately 530 Å. Both curves clearly show the presence of a longer-wavelength oscillation (beating) of a period of ≈0.2 Å^{-1}, which suggests the presence of a sublayer with a characteristic thickness of 30−40 Å. It follows that the film can be described as a system of two layers, one thick layer (≈495 Å) and a thinner one (≈40 Å). Among different two-layer configurations, the one with the thin layer close to the surface of the sample gave the best fit to the data, whereas other configurations, such as for instance with the thinner layer close to the substrate of the sample specimen, resulted in fits with lower quality. It should be noted that it was only when a fit using a single-layer model was found to be inadequate to fit the data [cf. Figure 3(a)], that a second layer was added, whereas models based on more than two layers did not improve the quality of the fits. The two layers are labeled as *Top layer* and *Bottom layer*, respectively, and a schematic depiction of the two-layer system is shown in Figure 4. One should note that the two sets of data were fitted independently

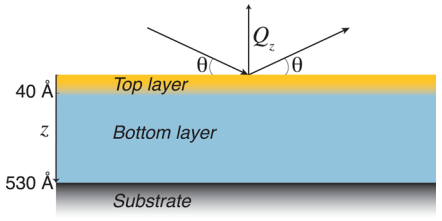

Figure 4. Schematic depiction of the specular reflectivity geometry and the double-layer model used to analyze the reflectivity data. The reflection angle is equal to the incident angle, and the scattering vector, Q_z, is perpendicular to the sample surface.

DOI: 10.1021/acs.jpcc.6b08570
J. Phys. Chem. C 2016, 120, 28415−28422

of each other. On the one hand, this method has the risk of leading to unphysical results since the two data sets are not completely independent. On the other hand, if, as in the case illustrated here, consistent parameters are obtained, such a fitting makes the parameters even more reliable since no agreement among the fit parameters is imposed.

In Table 1 the experimentally determined *e*SLDs are reported for the *Bottom layer*, for the hydrated and dehydrated

Table 1. Electron and Neutron SLD in the Bulk of the Sample (*Bottom Layer*) as Obtained from the Fit of the XRR and NR Data[a]

nominal condition	*e*SLD (10^{-6} Å^{-6})	*n*SLD (10^{-6} Å^{2})
hydrated	43.3 ± 0.8	3.2 ± 0.1
deuterated	—	4.0 ± 0.1
dehydrated	43.0 ± 0.8	3.4 ± 0.1

[a]The uncertainties for reported values are one standard deviation throughout the manuscript.

conditions of the film. It is worth noticing that the variation of the *e*SLD upon hydration is minimal, reflecting the fact that the atomic scattering factors of oxygen and hydrogen are small compared to the ones of Ba, Zr, and In. Of more relevance is the fact that the *e*SLDs for the *Top layer* are significantly lower than for the *Bottom layer*, for both the hydrated and dehydrated films [Figure 3(b)], indicating a difference in the chemical composition of the two layers, which is not (primarily) related to the degree of hydration. X-ray photoelectron spectroscopy measurements on one of the samples indicate a somewhat lower Ba concentration in the near-surface region, which could possibly explain this result, however, with a large uncertainty.

3.4. Neutron Reflectivity and *n*SLD Profiles. Figure 5(a) shows the NR data measured at the four different conditions of the film, i.e., hydrated, deuterated, and dehydrated, this last measured at both room temperature and 400 °C. The reflectivity curves are overall similar to each other, although small differences between the data for the four conditions can be observed, especially related to differences in the intensities of the Kiessig fringes. In agreement with the XRR data, the NR data are best described by a two-layer model characterized by a thinner layer close to the surface and a thicker layer beneath. It should be noted, however, that due to the limited Q_z-range combined with relatively low counting statistics the presence of a longer-wavelength oscillation superimposed on the shorter-wavelength Kiessig fringes is less clear than in the XRR data. The fits are shown by solid lines in Figure 5(a), whereas Figure 5(b) shows the corresponding *n*SLD profiles obtained from the fits. The *n*SLDs of the *Bottom layer* extracted from the fits are also shown in Table 1. The difference in *n*SLD for the three samples reflects the difference in coherent scattering length of H (−3.74 fm) and D (6.67 fm), thus confirming the insertion of H/D in the film. Similarly, the changes observed upon dehydration confirm the desorption of D/H. Judging from the magnitude of these changes, the bulk of the samples is considered to be fully hydrated/deuterated upon hydration/deuteration. The small differences in the *n*SLD profile of the *Bottom layer* of the sample upon the two different dehydrations are compatible with the uncertainties of the measurements and the effect of thermal expansion.

The *n*SLD of the *Top layer* is significantly lower than for the *Bottom layer*, similar to the *e*SLD measured by XRR due to the composition variations. The difference between the *n*SLD of

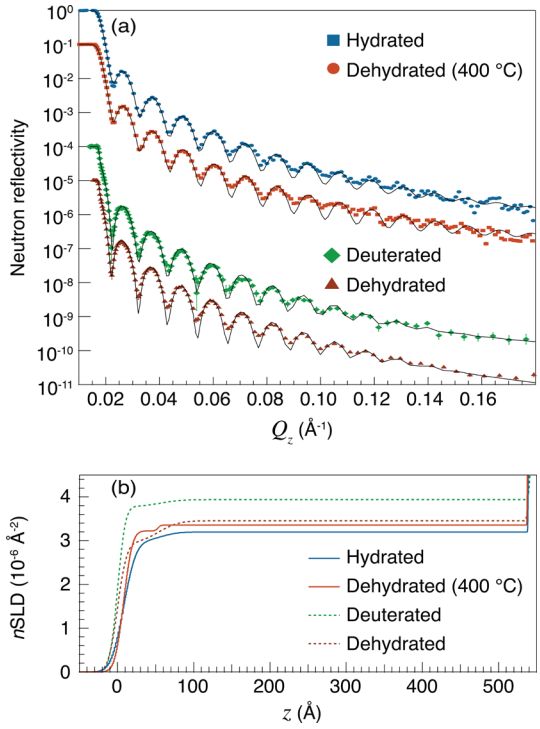

Figure 5. (a) NR data (points) and best fits (lines) for the 47In:BZO film in the four different experimental conditions. The reflectivity curves for the dehydrated (at 400 °C), deuterated, and dehydrated conditions have been scaled by 1, 4, and 5 orders of magnitude, respectively. (b) *n*SLD profiles as obtained from the fits based on the two-layer model.

the deuterated and hydrated condition is related to the H or D content. The *n*SLD is lower in the *Top layer* for the dehydrated condition at room temperature compared to the dehydrated condition at 400 °C, indicating greater residual H at room temperature in that layer.

3.5. Nuclear Reaction Analysis and Proton Concentration Depth Profile. Figure 6 shows the hydrogen concentration, [H], as obtained from the NRA measurements on nominally hydrated and dehydrated samples. Considering first the data for the hydrated sample, we observe a nonuniform distribution of H, specifically characterized by a larger

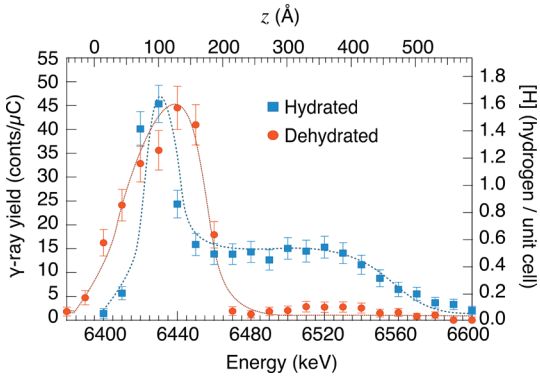

Figure 6. Energy profile of the γ-ray yield as measured for the hydrated and dehydrated 47In:BZO films. The estimated penetration depth is indicated on the top axis, whereas the H concentration, as estimated from the NR measurements, is shown on the right axis. Lines are guides to the eye.

DOI: 10.1021/acs.jpcc.6b08570
J. Phys. Chem. C 2016, 120, 28415−28422

concentration in the near-surface region of the film, whereas inside the bulk of the film the H concentration is homogeneous and significantly lower. Since the NR measurements suggest that the bulk of the sample is fully hydrated, the calibration of the NRA measurements was carried out assuming [H] = 0.47 (hydrogen/unit cell) in this region. This hydrogen concentration, calibrated in this way, is shown on the right axis of Figure 6. We should note that the presence of a large amount of hydrogen in the near-surface region cannot be explained by superficial water since in this case a peak width of only 13 keV is expected (see Figure S1) and not the 50 keV width as found in the present data. An important result is the fact that the dehydrated sample exhibits a large concentration of H in the near-surface region of the film, whereas in the bulk of the film essentially no protons can be observed. The thickness of this near-surface region is comparable with the thickness of the *Top layer* as extracted from the reflectivity measurements, and irrespectively, from the nominally hydrated or dehydrated condition of the sample, this region exhibits a H concentration significantly higher than that in the bulk of the hydrated sample. Notice that the somewhat thicker hydrogen-rich layer for the dehydrated sample compared to the hydrated one (Figure 6) may be an effect of the annealing (hydration) or just slight sample to sample variations.

4. DISCUSSION

To summarize our results, the XRR, NR, and NRA data are in excellent agreement, thus giving strong support for the existence of two distinct layers in epitaxial thin films of In-doped $BaZrO_3$, one hydrogen-rich layer close to the surface, with altered cationic composition, and a thicker layer, with a large difference in proton concentration between the hydrated and dehydrated conditions of the film. While the bulk of the film behaves as anticipated, the proton-rich near-surface layer, unexpectedly, either retains protons or reobtains protons after dehydration and cooling to room temperature. It follows that either a significant part of the protons are difficult/impossible to remove, even after high-temperature treatment in vacuum, and/or that the near-surface layer of the sample hydrates easily/quickly upon cooling to room temperature. Even though we cannot conclude what is the case, the observation of a slightly less H content of the *Top layer* at 400 °C as compared to its room-temperature value suggests that, at least some, reabsorption of protons is indeed taking place during the cooling of the sample to ambient conditions. Whatever the cause of protons also after dehydration, it is consistent with results from IR absorbance spectroscopy, which show the presence of a pronounced O−H stretch band in the ≈2000−3600 cm^{-1} range of the IR spectra,[6,8,27] and nuclear magnetic resonance[38] of the same or similar perovskite materials. The broad nature of the O−H stretch band reflects a distribution of different O−H bond distances, due to a range of different local proton sites in which the strength of hydrogen bonding to a neighboring oxygen atom, O−H···O, is different. In particular, variable-temperature IR absorbance data on $BaZr_{0.5}In_{0.5}O_{2.75+\delta}H_{2\delta}$ show a preferential desorption of protons in strongly hydrogen-bonding proton configurations (≈2000−2500 cm^{-1}) and that at above a temperature of ca. 350 °C protons in those strongly hydrogen-bonding configurations are essentially gone.[27] A comparison with our results suggests that the *Top layer* protons are associated with proton sites of relatively weak, or no, hydrogen bond character, while the bulk of the film relates also to a great deal of protons in sites characterized by strong/intermediate hydrogen bonding due to a variety of different local structures present, such as close/far to oxygen vacancies and/or dopant atoms.

The presence of different types of proton sites and in particular the inhomogeneous distribution of protons with the notable excess of protons in the *Top layer*, i.e., in the near-surface region of the film, raises the question whether the dynamics of these protons are different from protons in the bulk. This cannot be simply elucidated from the conductivity data because the conductivity as measured here reflects the charge-carrier mobility within the whole film, and therefore the contribution of proton conduction in the thin first 3−4 nm of the film to the total conductivity cannot be determined. Additionally, the high concentration of protons is likely to be characterized by pronounced proton−proton interactions that further complicate the development of a mechanistic understanding of the proton conductivity. Although our investigation concerns thin films, one should note that the accumulation of protons close to the surface should occur also in the crystallites of polycrystalline powder samples. The near-surface to volume ratio in polycrystalline samples increases going from micrometer-sized grains to nanometer-sized grains, for which in the latter case the ratio can be even larger than in the samples studied here. In this context, Groß et al.[39] and Beck et al.[40] investigated the effect of particle size on the atomic-scale proton diffusion in $BaZr_{0.85}M_{0.15}O_{2.925}$ (M = Y, In, and Ga) using quasielastic neutron scattering and found that when comparing the results from studies of micro- and nanocrystalline samples only the microcrystalline one showed a clear quasielastic signal related to proton motions, spatially localized in this case. It was suggested that in the nanocrystalline sample the protons are concentrated mainly to the surface and/or grain-boundary region of the crystallites, which is in agreement with our results. This is also in agreement with the lower conductivity of the GB compared to the bulk, but rather than being related to the appearance of a space-charge layer around the GB core, which leads to Schottky barriers and the depletion of mobile protons,[41,42] our results indicate that there is a slight composition variation that leads to the accumulation of protons in this region and, as a result, to proton configurations featured by lower proton mobility. The combination of our new results with the reported results from IR and neutron spectroscopy experiments, as discussed so far, would suggest a correlation between weak hydrogen-bonding interactions and low proton mobility, as found for the near-surface protons. In other words, our findings suggest that strong hydrogen-bonding interactions are important for high, at least localized, proton mobility. On a mechanistic level, this indicates that the proton jump process from one oxygen to another one, which is a hydrogen-bond-mediated process, is rate-limiting for the mobility, as opposed to the reorientational diffusion of the O−H group, which requires the breaking of hydrogen bonds.

5. CONCLUSIONS

We have carried out a comprehensive analysis of the structure, proton concentration depth profile, and conductivity of epitaxial, 50 nm thin films of In-doped $BaZrO_3$. The obtained proton conductivity and activation energy are comparable to literature values of bulk conductivity for similar materials, thus showing that grain-boundary conductivity is negligible due to the high crystallinity of the film. The presence of a 3−4 nm thick, proton-rich, near-surface layer with altered composition, likely related to some cationic deficiency, is observed. While

DOI: 10.1021/acs.jpcc.6b08570
J. Phys. Chem. C 2016, 120, 28415−28422

this layer either retains or reobtains protons after desorption and cooling to room temperature, the bulk of the film absorbs and desorbs protons in the expected manner. We suggest that the near-surface protons are located in proton sites characterized by relatively strong O−H bonds due to weak hydrogen-bond interactions to neighboring oxygen atoms and that the mobility of protons in these sites is generally lower than in proton sites associated with stronger hydrogen bonds; thus, strong hydrogen-bonding interactions are important for high proton mobility. Besides being of fundamental interest, these results are of relevance for the development of next-generation proton-conducting oxides with optimized proton conductivity and hence for the development of miniaturized SOFCs in actual operations that need to be periodically taken into and out of service (i.e., hydrated and dehydrated). Finally, our results demonstrate the applicability and potential of reflectivity techniques and NRA for gaining unique insight into the structural properties of proton-conducting oxide materials.

■ ASSOCIATED CONTENT

Supporting Information

The Supporting Information is available free of charge on the ACS Publications website at DOI: 10.1021/acs.jpcc.6b08570.

NRA and RBS spectra and a full list of author names in ref 31 (PDF)

■ AUTHOR INFORMATION

Corresponding Author

*Fax: +46 31 772 2090. Phone: +46 31 772 8038. E-mail: maths.karlsson@chalmers.se.

Notes

The authors declare no competing financial interest.

■ ACKNOWLEDGMENTS

This research was funded by the Swedish Research Council (grant No. 2008-6654 and No. 2010-3519) and by the Swedish Foundation for Strategic Research (grant No. ICAIO-0001). We also acknowledge the NIST Center for Neutron Research and the Institut Laue-Langevin for access to neutron beam facilities and the Tandem laboratory at Uppsala University for access to the ion beam instruments. The group of Ulrich Häussermann at Stockholm University is thanked for the spark plasma sintering.

■ REFERENCES

(1) Kilner, J. A.; Burriel, M. Materials for Intermediate-Temperature Solid-Oxide Fuel Cells. *Annu. Rev. Mater. Res.* **2014**, *44*, 365−393.

(2) Malavasi, L.; Fisher, C. A. J.; Islam, M. S. Oxide-ion and Proton Conducting Electrolyte Materials for Clean Energy Applications: Structural and Mechanistic Features. *Chem. Soc. Rev.* **2010**, *39*, 4370−87.

(3) Kreuer, K. D. Aspects of the Formation and Mobility of Protonic Charge Carriers and the Stability of Perovskite-Type Oxides. *Solid State Ionics* **1999**, *125*, 285−302.

(4) Kreuer, K. D. On the Development of Proton Conducting Materials for Technological Applications. *Solid State Ionics* **1997**, *97*, 1−15.

(5) Kreuer, K. D.; Adams, St.; Münch, W.; Fuchs, A.; Klock, U.; Maier, J. Proton Conducting Alkaline Earth Zirconates and Titanates for High Drain Electrochemical Applications. *Solid State Ionics* **2001**, *145*, 295−306.

(6) Ahmed, I.; Eriksson, S.-G.; Ahlberg, E.; Knee, C. S.; Berastegui, P.; Johansson, L.-G.; Rundlöf, H.; Karlsson, M.; Matic, A.; Börjesson, L. Synthesis and Structural Characterization of Perovskite Type Proton Conducting $BaZr_{1-x}In_xO_{3-\delta}$ ($0.0 \le x \le 0.75$). *Solid State Ionics* **2006**, *177*, 1395−1403.

(7) Ahmed, I.; Eriksson, S.-G.; Ahlberg, E.; Knee, C. S.; Johansson, L.-G.; Karlsson, M.; Matic, A.; Börjesson, L.; Götlind, H. Structural Study and Proton Conductivity in Yb-doped $BaZrO_3$. *Solid State Ionics* **2007**, *178*, 515−520.

(8) Ahmed, I.; Karlsson, M.; Eriksson, S.-G.; Ahlberg, E.; Knee, C. S.; Larsson, K.; Azad, A. K.; Matic, A.; Börjesson, L. Crystal Structure and Proton Conductivity of $BaZr_{0.9}Sc_{0.1}O_{3-\delta}$. *J. Am. Ceram. Soc.* **2008**, *91*, 3039−3044.

(9) Giannici, F.; Longo, A.; Balerna, A.; Kreuer, K.-D.; Martorana, A. Proton Dynamics in In:$BaZrO_3$: Insights on the Atomic and Electronic Structure from X-ray Absorption Spectroscopy. *Chem. Mater.* **2009**, *21*, 2641−2649.

(10) Fabbri, E.; Pergolesi, D.; Licoccia, S.; Traversa, E. Does the Increase in Y-dopant Concentration Improve the Proton Conductivity of $BaZr_{1-x}Y_xO_{3-\delta}$ Fuel Cell Electrolytes? *Solid State Ionics* **2010**, *181*, 1043−1051.

(11) Han, D.; Nose, Y.; Shinoda, K.; Uda, T. Site Selectivity of Dopants in $BaZr_{1-y}M_yO_{3-\delta}$ (M = Sc, Y, Sm, Eu, Dy) and Measurement of their Water Contents and Conductivities. *Solid State Ionics* **2012**, *213*, 2−7.

(12) Noferini, D.; Koza, M. M.; Fouquet, P.; Nilsen, G. J.; Kemei, M. C.; Rahman, S. M. H.; Maccarini, M.; Eriksson, S.; Karlsson, M. Proton Dynamics in Hydrated $BaZr_{0.9}M_{0.1}O_{2.95}$ (M = Y and Sc) Investigated with Neutron Spin-Echo. *J. Phys. Chem. C* **2016**, *120*, 13963.

(13) Karlsson, M.; Björketun, M. E.; Sundell, P. G.; Matic, A.; Wahnström, G.; Engberg, D.; Börjesson, L.; Ahmed, I.; Eriksson, S.; Berastegui, P. Vibrational Properties of Protons in Hydrated $BaIn_xZr_{1-x}O_{3-x/2}$. *Phys. Rev. B: Condens. Matter Mater. Phys.* **2005**, *72*, 094303.

(14) Karlsson, M.; Fouquet, P.; Ahmed, I.; Maccarini, M. Dopant Concentration and Short-Range Structure Dependence of Diffusional Proton Dynamics in Hydrated $BaIn_xZr_{1-x}O_{3-x/2}$ (x = 0.10 and 0.50). *J. Phys. Chem. C* **2010**, *114*, 3292−3296.

(15) Giannici, F.; Longo, A.; Kreuer, K.-D.; Balerna, A.; Martorana, A. Dopants and Defects: Local Structure and Dynamics in Barium Cerates and Zirconates. *Solid State Ionics* **2010**, *181*, 122−125.

(16) Yamazaki, Y.; Blanc, F.; Okuyama, Y.; Buannic, L.; Lucio-Vega, J. C.; Grey, C. P.; Haile, S. M. Proton Trapping in Yttrium-Doped Barium Zirconate. *Nat. Mater.* **2013**, *12*, 647−51.

(17) Jedvik, E.; Lindman, A.; Benediktsson, M. D.; Wahnström, G. Size and Shape of Oxygen Vacancies and Protons in Acceptor-Doped Barium Zirconate. *Solid State Ionics* **2015**, *275*, 2−8.

(18) Bjørheim, T. S.; Kotomin, E. A.; Maier, J. Hydration Entropy of $BaZrO_3$ from First Principles Phonon Calculations. *J. Mater. Chem. A* **2015**, *3*, 7639−7648.

(19) Steele, B. C. H.; Heinzel, A. Materials for Fuel-Cell Technologies. *Nature* **2001**, *414*, 345−52.

(20) Traversa, E. Toward the Miniaturization of Solid Oxide Fuel Cells. *Electrochem. Soc. Interface* **2009**, *18*, 49.

(21) Pergolesi, D.; Fabbri, E.; D'Epifanio, A.; Di Bartolomeo, E.; Tebano, A.; Sanna, S.; Licoccia, S.; Balestrino, G.; Traversa, E. High Proton Conduction in Grain-Boundary-Free Yttrium-Doped Barium Zirconate Films Grown by Pulsed Laser Deposition. *Nat. Mater.* **2010**, *9*, 846−52.

(22) Kim, Y. B.; Gür, T. M.; Jung, H.-J.; Kang, S.; Sinclair, R.; Prinz, F. B. Effect of Crystallinity on Proton Conductivity in Yttrium-Doped Barium Zirconate Thin Films. *Solid State Ionics* **2011**, *198*, 39−46.

(23) Higuchi, T.; Owaku, T.; Iida, Y.; Sakai, E.; Kobayashi, M.; Kumigashira, H. Proton Conduction of $BaCe_{0.90}Y_{0.10}O_{3-\delta}$ Thin Film with Lattice Distortion. *Solid State Ionics* **2015**, *270*, 1−5.

(24) Kreuer, K. Proton Conductivity: Materials and Applications. *Chem. Mater.* **1996**, *8*, 610−641.

(25) Ahmed, I.; Eriksson, S.-G.; Ahlberg, E.; Knee, C. S.; Karlsson, M.; Matic, A.; Engberg, D.; Börjesson, L. Proton Conductivity and Low Temperature Structure of In-doped $BaZrO_3$. *Solid State Ionics* **2006**, *177*, 2357−2362.

DOI: 10.1021/acs.jpcc.6b08570
J. Phys. Chem. C 2016, 120, 28415−28422

(26) Karlsson, M.; Matic, A.; Knee, C. S.; Ahmed, I.; Eriksson, S. G.; Börjesson, L. Short-Range Structure of Proton-Conducting Perovskite $BaIn_xZr_{1-x}O_{3-x/2}$ (x = 0−0.75). *Chem. Mater.* **2008**, *20*, 3480−3486.
(27) Karlsson, M.; Matic, A.; Zanghellini, E.; Ahmed, I. Temperature-Dependent Infrared Spectroscopy of Proton-Conducting Hydrated Perovskite $BaIn_xZr_{1-x}O_{3-x/2}$ (x = 0.10−0.75). *J. Phys. Chem. C* **2010**, *114*, 6177−6181.
(28) Certain products are identified to foster an understanding, which does not imply recommendation or endorsement by the National Institute of Standards and Technology nor does it imply that the materials or equipment identified are necessarily the best available for the purpose.
(29) Ahmed, I.; Knee, C. S.; Karlsson, M.; Eriksson, S.-G.; Henry, P. F.; Matic, A.; Engberg, D.; Börjesson, L. Location of Deuteron Sites in the Proton Conducting Perovskite $BaZr_{0.50}In_{0.50}O_{3-y}$. *J. Alloys Compd.* **2008**, *450*, 103−110.
(30) Björck, M.; Andersson, G. GenX: an Extensible X-ray Reflectivity Refinement Program Utilizing Differential Evolution. *J. Appl. Crystallogr.* **2007**, *40*, 1174−1178.
(31) Dura, J. A.; Pierce, D. J.; Majkrzak, C. F.; Maliszewskyj, N. C.; McGillivray, D. J.; Lösche, M.; O'Donovan, K. V.; Mihailescu, M.; Perez-Salas, U.; Worcester, D. L.; et al. AND/R: Advanced Neutron Diffractometer/Reflectometer for Investigation of Thin Films and Multilayers for the Life Sciences. *Rev. Sci. Instrum.* **2006**, *77*, 74301.
(32) Kienzle, P.; O'Donovan, K.; Ankner, J.; Berk, N.; Majkrzak, C. F. *Reflpak*, 2000; http://www.ncnr.nist.gov/reflpak/.
(33) Cubitt, R.; Fragneto, G. D17: the New Reflectometer at the ILL. *Appl. Phys. A: Mater. Sci. Process.* **2002**, *74*, s329−s331.
(34) Nelson, A. Co-refinement of Multiple-Contrast Neutron/X-ray Reflectivity data using MOTOFIT. *J. Appl. Crystallogr.* **2006**, *39*, 273−276.
(35) Daillant, J., Gibaud, A., Eds. *X-ray and Neutron Reflectivity*; Lecture Notes in Physics; Springer Berlin Heidelberg: Berlin, Heidelberg, 2009; Vol. *770*.
(36) Parratt, L. Surface Studies of Solids by Total Reflection of X-Rays. *Phys. Rev.* **1954**, *95*, 359−369.
(37) Wilde, M.; Fukutani, K. Hydrogen Detection Near Surfaces and Shallow Interfaces with Resonant Nuclear Reaction Analysis. *Surf. Sci. Rep.* **2014**, *69*, 196−295.
(38) Oikawa, I.; Takamura, H. Correlation among Oxygen Vacancies, Protonic Defects, and the Acceptor Dopant in Sc-Doped $BaZrO_3$ Studied by ^{45}Sc Nuclear Magnetic Resonance. *Chem. Mater.* **2015**, *27*, 6660−6667.
(39) Groß, B.; Beck, C.; Meyer, F.; Krajewski, T.; Hempelmann, R.; Altgeld, H. $BaZr_{0.85}Me_{0.15}O_{2.925}$ (Me = Y, In and Ga): Crystal Growth, High-Resolution Transmission Electron Microscopy, High-Temperature X-ray Diffraction and Neutron Scattering experiments. *Solid State Ionics* **2001**, *145*, 325−331.
(40) Beck, C.; Janssen, S.; Groß, B.; Hempelmann, R. Neutron Time-Of-Flight Spectrometer FOCUS at SINQ: Results from Nanocrystalline Matter Studies. *Scr. Mater.* **2001**, *44*, 2309−2313.
(41) Chen, C.-T.; Danel, C. E.; Kim, S. On the Origin of the Blocking Effect of Grain-Boundaries on Proton Transport in Yttrium-Doped Barium Zirconates. *J. Mater. Chem.* **2011**, *21*, 5435.
(42) Shirpour, M.; Merkle, R.; Lin, C. T.; Maier, J. Nonlinear Electrical Grain Boundary Properties in Proton Conducting Y−$BaZrO_3$ supporting the Space Charge Depletion Model. *Phys. Chem. Chem. Phys.* **2012**, *14*, 730−740.

DOI: 10.1021/acs.jpcc.6b08570
J. Phys. Chem. C 2016, 120, 28415−28422